







Imaging symmetric and antisymmetric behavior of orbital-angular-momentum-entangled two-photon states

Zeferino Ibarra-Borja ^{1,2}, Pablo Yepiz-Graciano ^{1,2}, Nicolas Claro-Rodríguez ¹,
Alfred B. U'Ren ² and Roberto Ramírez-Alarcón ^{1,*}

¹*Centro de Investigaciones en Óptica A. C., León, Guanajuato 37150, Mexico*

²*Instituto de Ciencias Nucleares, Universidad Nacional Autónoma de México, CDMX 04510, Mexico*

 (Received 21 March 2024; revised 12 July 2024; accepted 29 July 2024; published 27 August 2024)

We report on an experiment in which orbital-angular-momentum (OAM)-entangled photon pairs generated by the spontaneous parametric down-conversion process can be engineered to have particular symmetry properties. Our method is based on the use of a Dove-prism pair in conjunction with Hong-Ou-Mandel (HOM) interferometry resolved in transverse position and OAM. The latter allows us to engineer the postselected two-photon state to exhibit a specific type of symmetry. By selecting particular topological charge values for the pump and for the postselected two-photon state, we can transition from a symmetric two-photon state and a HOM dip to an antisymmetric state and a HOM peak. Spatial resolution allows us to obtain the HOM interferogram both at the single-pixel level and globally by summing over all sensor pixels. Furthermore, through spatially selective OAM projection of the detected photon pairs, we can define multiple transverse regions with different symmetry properties, as verified by our spatially resolved HOM apparatus. Although we used two transverse regions for this proof-of-concept demonstration, this method could in principle be scaled to a larger number of regions, leading to a new technique to be added to the existing toolbox for quantum technologies in the photonic domain.

DOI: [10.1103/PhysRevApplied.22.024068](https://doi.org/10.1103/PhysRevApplied.22.024068)

I. INTRODUCTION

In the past few decades, much progress has been made in studying quantum optical effects from the perspective of the interplay of different photonic degrees of freedom, such as frequency and time, transverse position, and orbital angular momentum (OAM). Among different photonic degrees of freedom, OAM has attracted significant attention on account of the very broad range of related applications that have been demonstrated, including in optical trapping [1–3], optical manipulation [4], and communications [5]. Specifically, in the context of quantum technology implementations based on photons, OAM has emerged as a photonic degree of freedom with great promise because it leads to discrete Hilbert spaces which, unlike polarization, permits a scalable effective dimensionality [6]. Indeed, for photon-pair sources based on the process of spontaneous parametric down-conversion (SPDC), it becomes possible to tailor the spiral bandwidth, i.e., the range of topological charge values available in the photon-pair state [7,8], leading to the possibility of encoding more than one bit of information per photon. The resulting high-dimensional OAM-entangled photon pairs produced by SPDC can lead to a number of applications [6,9], for

example in the context of quantum cryptography [10]. Furthermore, the possibility of transmitting such high-dimensional entanglement [11] enhances its applicability to the development of future communication networks.

In addition to the scalability in the Hilbert-space dimension for OAM-entangled photon pairs described above, numerous recent studies have explored the properties of spatially entangled photon pairs as revealed by Hong-Ou-Mandel (HOM) interferometry, for example involving hyperentangled states [12], high-dimensional spatial modes [13], and spin-orbit entangled photons [14]. Furthermore, the possibility of controlling the degree of coherence of photons was demonstrated in a recent study [15], and a quantum imaging technique exploiting twisted photons has also been developed [16]. Nevertheless, an interesting avenue of research involves the ability to achieve qualitative control over the OAM-entangled state, specifically through its symmetry properties. When described in terms of the Laguerre-Gaussian modes, the SPDC OAM-entangled two-photon state can be written as a superposition of the $|\Psi^+\rangle$ symmetric Bell states [17], for which the symmetry of the state implies invariance under photon permutation. Interestingly, in Ref. [18], it was shown that it is possible to apply a symmetry transformation to the SPDC two-photon state to convert the symmetric $|\Psi^+\rangle$ state to the antisymmetric $|\Psi^-\rangle$ Bell state through

*Contact author: roberto.ramirez@cio.mx

the use of a Dove-prism pair. Such symmetry control has enabled the development of several applications, including high-dimensional quantum gates [19,20] and symmetry-selective ghost imaging [21,22].

It is well known that the bunching and/or antibunching behavior in HOM interference in a beam splitter is intimately tied to the symmetry properties of the incoming photon pairs. It is therefore no surprise that a HOM interferometer may be used specifically in the context of OAM-entangled photon pairs to probe the effects of symmetry transformations executed with a Dove-prism pair. In this paper, we extend previous work showing that a Dove-prism pair can be used to control photon-pair symmetry and the resulting HOM interference. While HOM interference is traditionally visualized as being dependent on the temporal delay between the signal and idler photons, we report here on a HOM interferometer device in which the interference is resolved not only in delay but also in transverse position and OAM topological charge (through postinterference selective OAM projection). We detect one of the two photons in each pair with a time-gated intensified coupled charge device (ICCD), which exhibits single-photon sensitivity at each pixel, enabling us to observe HOM interference either at the individual-pixel level or “globally” by summing up all ICCD pixel readouts. On the one hand, we show that extending the HOM apparatus to include OAM resolution allows us, in a specific configuration, to alternate between an interference dip and peak as the projected topological charge ℓ is increased. On the other hand, we demonstrate that projecting OAM in a transversely spatially selective manner allows us to engineer the postselected state to exhibit transverse regions with different types of symmetry, as evidenced by our spatially resolved HOM apparatus. Although the photon pairs in our proof-of-concept demonstration exhibit up to two such regions, this could in principle be scaled to a larger number of regions, paving the way for extending the information content of photon pairs for quantum communication protocols.

II. THEORY

A. OAM state engineering

The state produced by SPDC can be expressed as a superposition of symmetric Bell states, entangled in the OAM degree of freedom, as follows:

$$|\Psi\rangle = \sum_{\ell} a_{\ell} |\Psi_{\ell, \ell_p - \ell}^+\rangle, \quad (1)$$

where

$$|\Psi_{\ell, \ell_p - \ell}^+\rangle = \frac{1}{\sqrt{2}} (|\ell\rangle_s |\ell_p - \ell\rangle_i + |\ell_p - \ell\rangle_s |\ell\rangle_i), \quad (2)$$

in which ℓ_p , $\ell_s = \ell$, and $\ell_i = \ell_p - \ell$ are the values of the topological charge for the pump (p), signal (s), and idler (i) photons, respectively. Note that because only the azimuthal mode index is controlled in our experiment, if expanded in the Laguerre-Gauss basis, a $|\ell\rangle$ state represents, in fact, a superposition of the various radial modes [17].

When a Laguerre-Gaussian mode $|\ell\rangle$ with topological charge ℓ is transmitted through a sequence of two Dove prisms with a relative angle ϕ between them, it is transformed as $|\ell\rangle \rightarrow |\ell\rangle e^{i2\ell\phi}$. It may be shown that this implies that upon transmission of the signal photon through the Dove prisms, the SPDC state becomes [18]

$$|\Psi\rangle = \sum_{\ell} a_{\ell} \left(\cos((2\ell - \ell_p)\phi) |\Psi_{\ell, \ell_p - \ell}^+\rangle + i \sin((2\ell - \ell_p)\phi) |\Psi_{\ell, \ell_p - \ell}^-\rangle \right), \quad (3)$$

where the state is expressed in terms of the symmetric (indicated with $+$) and antisymmetric (indicated with $-$) $|\Psi^{\pm}\rangle$ Bell states, given by $|\Psi_{\ell, \ell_p - \ell}^{\pm}\rangle = \frac{1}{\sqrt{2}} (|\ell\rangle_s |\ell_p - \ell\rangle_i \pm |\ell_p - \ell\rangle_s |\ell\rangle_i)$.

In an experimental situation, it is possible to directly control the topological charge of the pump ℓ_p (in our particular experiment, see below, we use $\ell_p = 0$). In addition, one of the SPDC photons can be projected to a certain topological charge value ℓ before detection. In effect, this limits the sum in Eqs. (1) and (3) to a single ℓ value through postselection. In this manner, both ℓ_p and ℓ may be considered as experimental variables that may be selected freely.

From Eq. (3), it becomes evident that we can control the relative weights of the symmetric and antisymmetric state components through the interprism angle ϕ , along with the selected values of the pump and SPDC photon topological charges ℓ_p and ℓ . For example, by setting $\phi = 0^\circ$, the output state becomes purely symmetric, regardless of the values of ℓ and ℓ_p . Conversely, setting $\ell_p = 0$ and $\ell = 0$ produces a purely symmetric state irrespective of the angle ϕ .

In general, the question arises of how the choice of the three parameters ℓ_p , ℓ , and ϕ translates into specific weights for the symmetric and antisymmetric state components. With this purpose in mind, we have prepared the diagrams in Fig. 1, in which we first fix the value of ℓ_p [to 0 and 1 in panels (a) and (b), respectively]. The value selected for ℓ (with $\ell \geq 1$; the case $\ell = 0$ is considered separately) then defines the radius of a circumference along which we use the coefficients for the states $|\Psi_{\ell, \ell_p - \ell}^+\rangle$ and $|\Psi_{\ell, \ell_p - \ell}^-\rangle$ to define a point in such a manner that if it lies on the horizontal (vertical) axis, the resulting state is purely symmetric (antisymmetric). We can then plot the resulting points for a given fixed angle ϕ , for all possible ℓ values (in

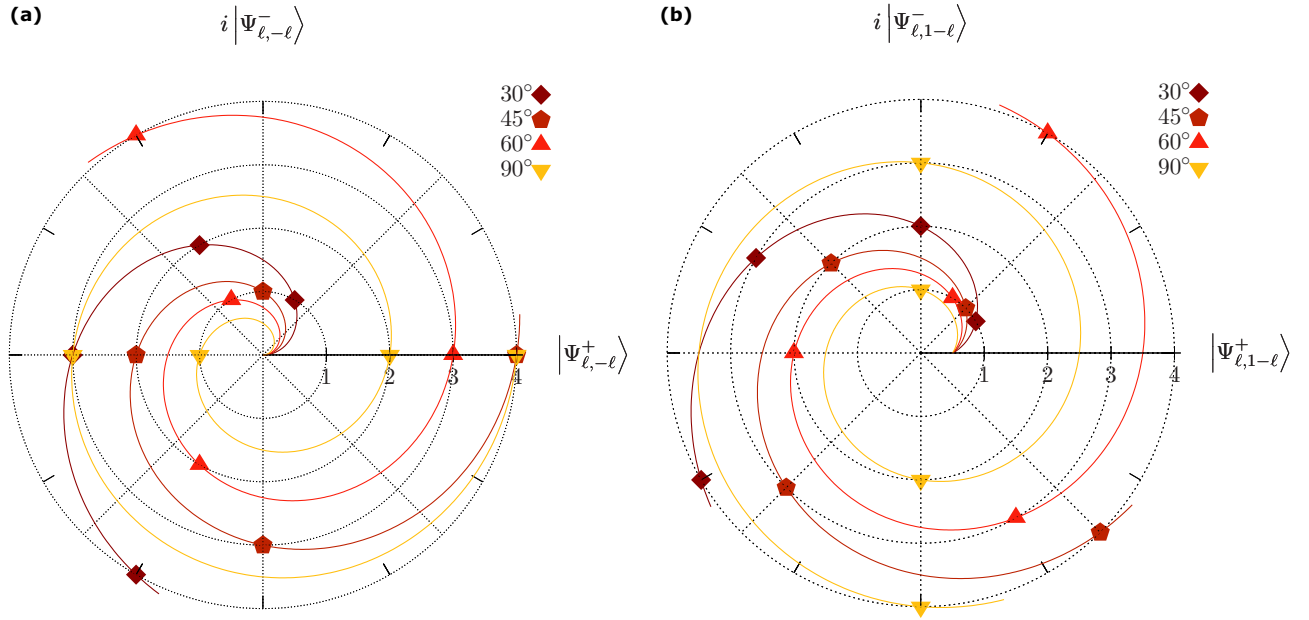


FIG. 1. Polar diagrams showing the properties of the postselected SPDC state for (a) $\ell_p = 0$ and (b) $\ell_p = 1$. The radius of the polar diagram (indicated in the horizontal axis) represents the SPDC topological charge projection value ℓ . Along a circumference for a specific ℓ , the symmetric and antisymmetric coefficients define a point, and if this lies on the horizontal (vertical) axis, the postselected state is purely symmetric (antisymmetric). Points defined by the same interprism angle ϕ are joined together smoothly to form the spiral shapes shown.

this case with $1 \geq \ell \geq 4$). Using a certain marker symbol and color for each angle ϕ (green diamonds for $\phi = 30^\circ$, red pentagons for $\phi = 45^\circ$, orange triangles for $\phi = 60^\circ$, and inverted yellow triangles for $\phi = 90^\circ$), and including lines to smoothly connect like markers, we obtain the spiral shapes shown in the diagrams. Note that the special case $\ell_p = \ell = 0$ leads to a trajectory coinciding with the (positive) horizontal axis.

Let us discuss a few specific cases of interest stemming from Fig. 1. First, as already addressed in Ref. [18], for a pump beam with $\ell_p = 0$ (Gaussian beam) and $\phi = 45^\circ$ [red pentagons in Fig. 1(a)], each even (odd) ℓ index generates a symmetric (antisymmetric) state. For $\ell_p = 1$ and $\phi = 90^\circ$ [yellow triangles in Fig. 1(a)], the output state is antisymmetric for all ℓ -index values. Finally, for $\ell_p = 1$ and $\phi = 45^\circ$ [red pentagons in Fig. 1(a)], the resulting symmetric and antisymmetric contributions are equal for all ℓ values.

1. Hong Ou Mandel interferometry as a symmetry filter

It is well known that HOM interference can act as a symmetry filter [18] because while symmetric states produce the characteristic HOM dip due to photon bunching, antisymmetric states produce a HOM peak due to anti-bunching. The visibility of the HOM interferometer can be defined as follows [23]:

$$v = \frac{p_c(0) - p_c(\infty)}{p_c(\infty)}, \quad (4)$$

where $p_c(0)$ is the coincidence probability at zero path difference $\tau = 0$ and $p_c(\infty) = 0.5$ is the long-delay coincidence probability (for $|\tau| \rightarrow \infty$). The fact that the state $|\Psi_{\ell,\ell_p-\ell}^+\rangle$ leads to an interference dip (with a null in coincidences at $\tau = 0$) and the state $|\Psi_{\ell,\ell_p-\ell}^-\rangle$ leads to an interference peak (with unit coincidence probability at $\tau = 0$), can be used to derive the following expression for the HOM visibility as a function of the parameters ℓ_p , ℓ , and ϕ (see the Appendix for its derivation):

$$v = 2 \sin^2((2\ell - \ell_p)\phi) - 1. \quad (5)$$

Note that we are using a sign convention such that when using Eq. (5), a positive (negative) value for v indicates an overall state asymmetry (symmetry) leading to an interference peak (dip).

III. EXPERIMENT

Our experimental setup is shown in Fig. 2. The pump beam (PB) is a narrowband laser at 405 nm with 70 mW power. This is spatially filtered by coupling into a single-mode fiber (SMF₁) with an 8-mm-focal-length aspheric lens (AL₁), thus retaining only the $\ell_p = 0$ component. It is subsequently outcoupled back to free space with another 8-mm aspheric lens (AL₂). The resulting beam, to be used as a pump for the SPDC process, is then spectrally filtered by a colored filter (BG39 from Schott; DF) to suppress background photons, and it is focused with the help of a 1000-mm-focal-distance lens (L_1) to

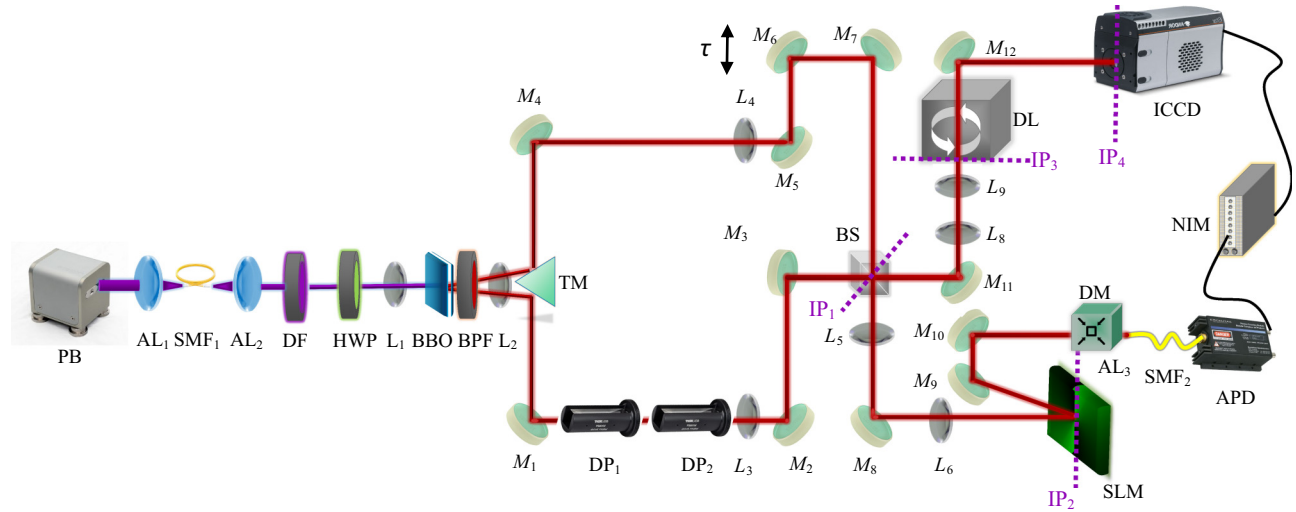


FIG. 2. Experimental setup. OAM-entangled photon pairs are generated by the SPDC process. The signal photon is transmitted through a Dove-prism pair (DP₁ and DP₂) to manipulate the properties of the resulting photon pair, and the photon pairs interfere in a beam splitter (BS). While one of the photons emerging from the BS is spatially resolved upon detection by an ICCD camera, upon transmission through the image-preserving optical delay line (DL), the other photon is projected to a user-selected topological charge value prior to detection by an avalanche photodiode (APD).

a waist of $\sim 120\text{-}\mu\text{m}$ radius at the crystal plane. In addition, the polarization is controlled by a half-wave plate (HWP) to maximize the SPDC generation rate. A beta barium borate (BBO) crystal of 2-mm thickness is illuminated by the pump beam to produce noncollinear, frequency-degenerate photon pairs through type-I SPDC. The bandwidth of the signal and idler photons is restricted by transmission through a $810 \pm 5\text{-nm}$ bandpass filter (FBH810-10 from Thorlabs; BPF) with a rectangular transmission window.

The noncollinear trajectories of the SPDC photon pairs (at $\pm 1.5^\circ$ emission angles with respect to the pump axis) are further separated by a triangular mirror. The signal and idler photons produced at the crystal are separately imaged, using a $4f$ system acting on each of the two photons, to the plane of the beam splitter (BS), labeled as the image plane IP₁, where HOM interference takes place. The signal-photon $4f$ system consists of lenses L_2 (focal length $f_2 = 150$ mm) and L_3 (focal length $f_3 = 500$ mm), so that the BBO- L_2 , L_2 - L_3 , and L_3 -BS separations are f_2 , $f_2 + f_3$, and f_3 , respectively. Likewise, the idler-photon $4f$ system consists of lenses L_2 (focal length $f_2 = 150$ mm) and L_4 (focal length $f_4 = 500$ mm), so that the BBO- L_2 , L_2 - L_4 , and L_4 -BS separations are f_2 , $f_2 + f_4$, and f_4 , respectively. Before reaching the BS, while the signal photon is transmitted through two Dove prisms (DP_{1,2}) with an interprism angle ϕ , the idler photon is reflected from two mirrors (M_6 and M_7) mounted on a translatable computer-controlled stage (with 25 mm travel and 100 nm minimum step) to introduce a controllable temporal delay τ between the signal and idler photons, as is required for HOM interferometry.

An important feature of our experimental design is that the HOM interference is resolved in three distinct experimental variables: (i) spatially on the transverse plane, (ii) in the OAM topological charge, and (iii) in the signal-idler temporal delay. For this purpose (see below), while the photon exiting the beam splitter through output port 1 is subjected to postinterference OAM projection, the photon exiting through output port 2 is detected in a spatially resolved manner.

The photon exiting the beam splitter through output port 1 is imaged to the input plane (IP₂) of an OAM projection module using a $4f$ system comprising lenses L_5 and L_6 (both with focal length $f_5 = f_6 = 250$ mm), so that the BS- L_5 , L_5 - L_6 , and L_6 -spatial light modulator (SLM) separations are f_5 , $f_5 + f_6$, and f_6 , respectively. The OAM projection module consists of an SLM followed by three consecutive demagnifying $4f$ telescopes with total magnification $\times 0.0015$, which couples the photon into a single-mode fiber (SMF₂). The magnifications are: $\times 0.4$ formed by lenses with focal lengths of 250 and 100 mm, $\times 0.24$ formed by lenses with focal lengths 250 and 60 mm, and $\times 0.016$ formed by a lens with focal length 500 mm combined with an aspheric lens (AL₃) with focal length 8 mm; this succession of three telescopes is indicated in Fig. 2 by the box labeled DM. The purpose of the SLM is to selectively convert, through the use of an appropriate fork-shaped hologram displayed on the SLM screen, the portion of the incoming light that is characterized by a topological charge ℓ to a Gaussian mode (with $\ell = 0$) that can couple well to a single-mode fiber, thus effectively suppressing other incoming ℓ values. The end result is the projection of the mode exiting the BS through output port 1

to a specific desired topological charge ℓ prior to detection at an avalanche photodiode (APD) module.

The photon exiting the BS through output port 2 is spatially resolved upon detection by an ICCD camera with a resolution of 1024×1024 pixels. This leads to the ability to visualize the HOM interference resolved on the transverse plane as the signal-idler delay is varied. For this purpose, the photon exiting the BS through output port 2 is first imaged to the input plane IP_3 of an image-preserving optical DL, which is about 28 m long (approximately 90 ns) and is designed to overcompensate for the insertion delay time of the ICCD camera. This allows us to obtain the full portion of interest from the HOM interferogram. The photon on plane IP_3 is then relayed to plane IP_4 , which corresponds with the ICCD sensor. Each detection event at the APD produces an electronic pulse, which is discriminated and electronically adjusted with a nuclear instrumentation module (NIM) discriminator to define a ~ 5 -ns detection window at the ICCD camera, enabling us to acquire spatially resolved coincidence counts. By scanning the signal-idler delay τ , we are then able to obtain the spatially- and OAM-resolved HOM interferogram.

Note that while the interprism angle ϕ can be chosen freely, for the experimental results shown here, we have used the value $\phi = 45^\circ$. As has already been discussed in the context of Fig. 1(a), for a Gaussian pump (with $\ell_p = 0$), this value of ϕ allows us to alternate between a

fully symmetric state for $\ell = 0, 2, 4$ (and similarly for all even values) and a fully asymmetric state for $\ell = 1, 3$ (and similarly for all odd values).

A. Symmetric behavior

An initial experiment with a purely symmetric state involves the use of a Gaussian pump ($\ell_p = 0$) and an SPDC photon projection $\ell = 0$. As mentioned above, for this choice of ℓ_p and ℓ , the state is symmetric irrespective of the interprism angle ϕ , leading to an in-principle unit-visibility HOM dip.

In Fig. 3, we present our experimental results for this configuration. Figure 3(b) shows the HOM interferogram for temporal delay τ values ranging from -200 fs ($-60 \mu\text{m}$) to $+200$ fs ($+60 \mu\text{m}$). While the red dots correspond to the interferogram obtained by summing over all ICCD pixels, the black dots correspond to the interferogram obtained for a single pixel (see below). Note that the shape of the HOM interferogram is defined by the Fourier transform of the photon-pair spectral distribution interfering at the beam splitter (BS element). In our case, the photon pairs are spectrally shaped by the BPF element (FBH810-10 from Thorlabs), which presents a spectral transmission function with a nearly rectangular shape. Considering the Fourier-transform properties of rectangular functions, this suggests that an excellent candidate for

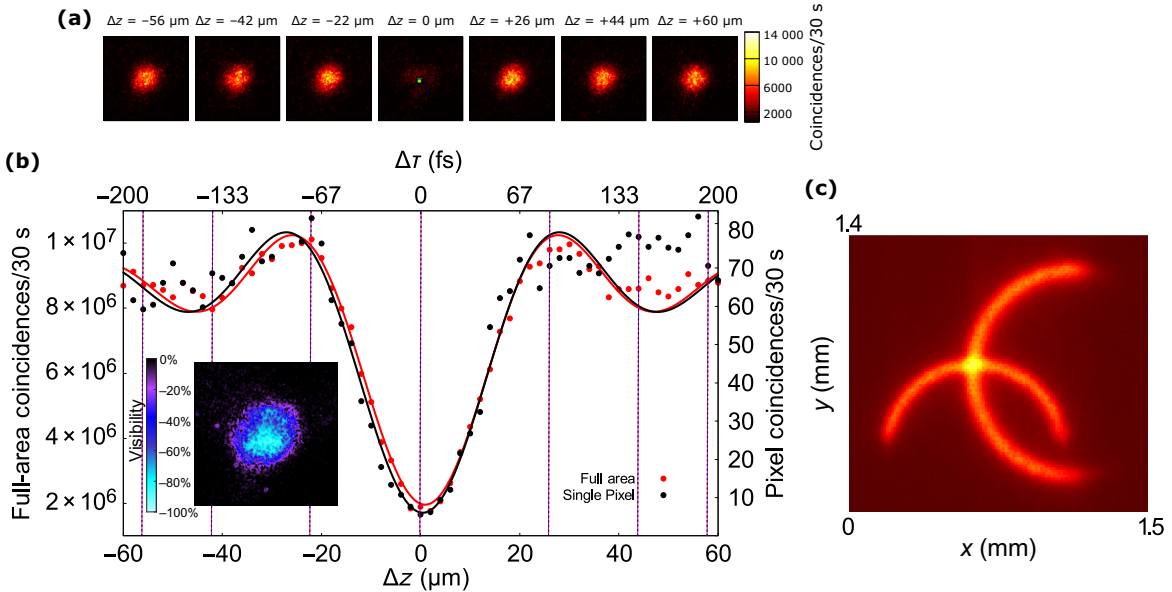


FIG. 3. HOM interference behavior for $\ell_p = \ell = 0$ and $\phi = 45^\circ$. Panel (a) shows the spatially resolved HOM interferograms for a selection of seven different signal-idler τ values, with the case $\tau = 0$ corresponding to the central plot; the green dot in this plot indicates the pixel used for the single-pixel interferogram, as described in the main text. (b) Single-pixel HOM interferogram (black dots), along with the global interferogram obtained by summing over all ICCD pixel readouts (red dots), for temporal delay τ values ranging from -200 fs ($-60 \mu\text{m}$) to $+200$ fs ($+60 \mu\text{m}$). The curves are fits to sinc-squared functions for comparison purposes only, as detailed in the main text. (c) Transverse intensity of the two portions of the SPDC ring (for each of the signal and idler photons) clipped by the triangular mirror, one of which is rotated by the Dove-prism pair. The image shown was taken on the plane of the BS (IP_1) and has dimensions of $1.5 \text{ mm} \times 1.4 \text{ mm}$ (119×110 pixels of the ICCD sensor).

fitting the HOM dip profile is a sinc-squared function. The black (red) curve represents such a fit for the single pixel (full-area) cases [24]. It is interesting to note that the interferograms for the single-pixel and summed-pixel cases are essentially identical, with visibilities $\sim 81.6\%$ and $\sim 80.9\%$, respectively, i.e., manifesting a clearly symmetric behavior in both cases. The inset of Fig. 3(b) shows the spatially resolved HOM visibility, revealing a considerable transverse area with visibilities very similar to those obtained by adding up all pixels. Note that the visibility becomes essentially zero—as one would expect—in areas where the state amplitude is negligible. The ability to obtain the local visibility in the spatially resolved HOM interference, suggests the possibility of defining areas with different symmetry properties to encode more information per photon; this idea is developed in a later section of this paper.

Note also that the visibility is somewhat lower than the ideal unity value on account of the difficulty of aligning the two halves of the type-I SPDC ring (for the signal and idler photons) defined by the reflection from the two faces of the triangular mirror. Upon reflection, the signal-mode half-ring intensity distribution is rotated on the transverse plane by a pair of Dove prisms before overlapping with

the unrotated idler-mode half-ring intensity distribution at the BS. In Fig. 3(c), we show the far-field transverse intensity distribution of the two overlapping ring halves, as measured with a CCD camera on the BS plane IP_1 .

Figure 3(a) shows the spatially resolved coincidence count rate for a selection of seven specific delay values; note that the spatial structure for nonzero delay values corresponds well with a Gaussian $\ell = 0$ mode, as would be expected. Note that in the case of zero delay [$\Delta z = 0$; central plot in Fig. 3(a)], the green pixel represents that selected (with the criterion of being near the intensity maximum) for the single-pixel interferogram [displayed as black dots in Fig. 3(b)].

B. Antisymmetric behavior

Following the red curve marked with red pentagons in Fig. 1(a), which corresponds to an interprism angle of $\phi = 45^\circ$, it is clear that for $\ell = 1$ (and $\ell_p = 0$), antisymmetric behavior with a HOM peak is expected. Our experimental data for this case is shown in Fig. 4, which has a similar structure to Fig. 3, as discussed above for the symmetric case. In Fig. 4(b), we show the summed-pixel and individual-pixel HOM interferograms for temporal delay τ values ranging from -200 fs (-60 μm) to $+200$ fs

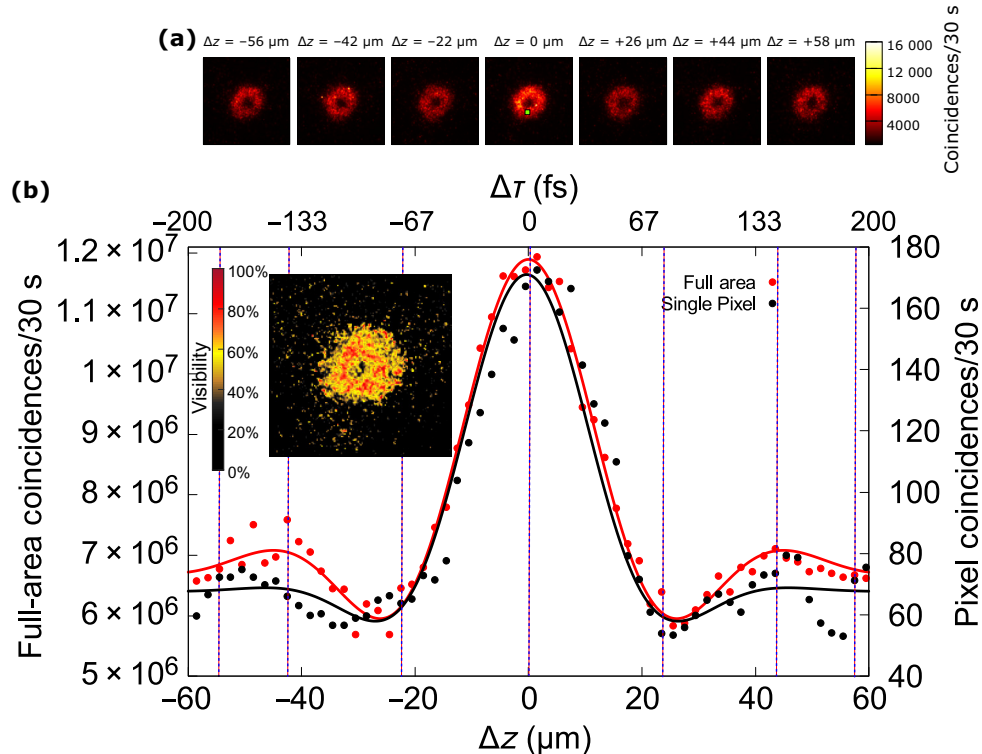


FIG. 4. HOM interference behavior for $\ell_p = 0$, $\ell = 1$, and $\phi = 45^\circ$. Panel (a) shows the spatially resolved HOM interferograms for a selection of seven different signal-idler τ values, with the case $\tau = 0$ corresponding to the central plot; the green dot in this plot indicates the pixel used for the single-pixel interferogram, as described in the main text. (b) Single-pixel HOM interferogram (black dots), along with the global interferogram obtained by summing over all ICCD pixel readouts (red dots), for temporal delay τ values ranging from -200 fs (-60 μm) to $+200$ fs ($+60$ μm). The curves are fits to sinc-squared functions for comparison purposes only.

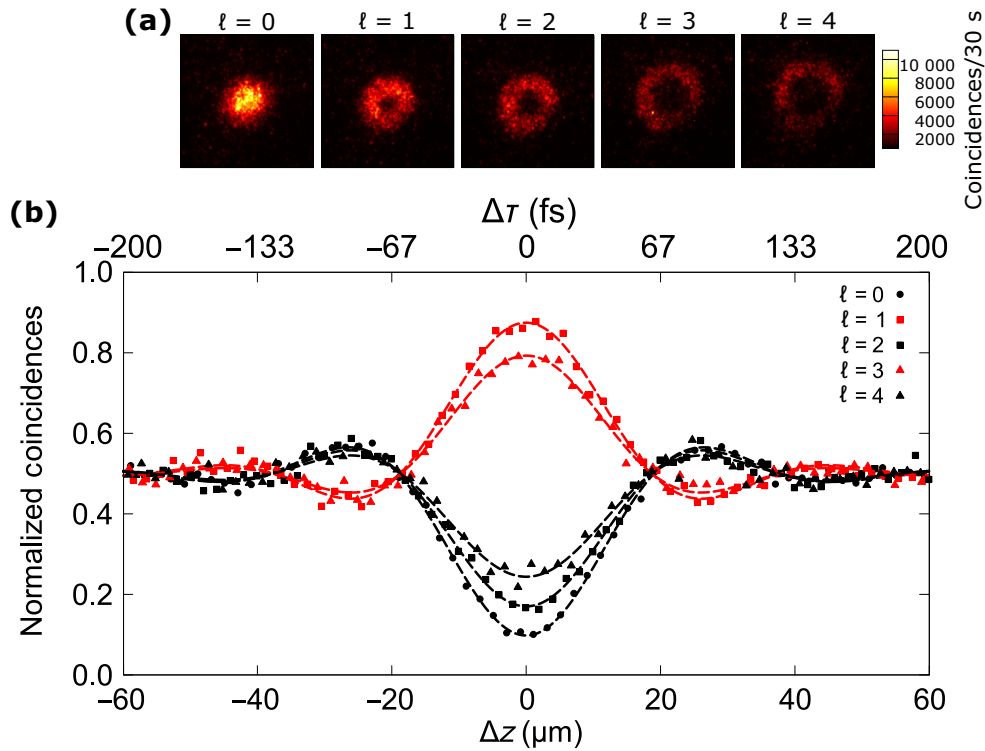


FIG. 5. HOM interference behavior for $\ell_p = 0$ and $\ell = 0, 1, 2, 3, 4$ and $\phi = 45^\circ$. Panel (a) shows the spatially resolved HOM interferograms at a delay value corresponding to $\Delta z = -56 \mu\text{m}$ ($\tau = -186 \text{ fs}$) outside of the dip/peak area for each value of ℓ . Panel (b) shows the HOM interferograms for $\ell = 0, 1, 2, 3, 4$, demonstrating an alternation between dips (for $\ell = 0, 2, 4$) and peaks (for $\ell = 1, 3$).

(+60 μm) with red and black dots, respectively, yielding corresponding visibilities of 74.7% and 72.5%. As was the case for the symmetric state, these two interferograms are essentially identical; again, the black (red) lines are fits to sinc-squared peak-profile functions for the single-pixel (full-area) cases. The inset of Fig. 4(b) shows the spatially resolved visibility, exhibiting a broad transverse area for which the visibility is similar to that corresponding to the summed-up pixels.

Figure 4(a) shows the spatially resolved coincidence counts for a selection of seven temporal-delay values, showing good correspondence with the expected structure for an $|\ell\rangle$ mode with $\ell = 1$ topological charge (particularly exhibiting a phase singularity). Note that the central plot exhibits a higher count rate compared to its neighbors, as one would expect from the fact that a coincidence peak is observed. Note also that the specific pixel colored green in the central plot of the top panel is the one that was selected for the single-pixel HOM interference (with the criterion of being near the midway point through the width of the intensity ring, in its lower portion) in Fig. 4(b).

C. HOM interference for higher ℓ values

As has already been pointed out, an experimental configuration with $\ell_p = 0$ and interprism angle $\phi = 45^\circ$ leads

for each even (odd) ℓ index to the generation of a symmetric (antisymmetric) state, as indicated by the red pentagons in Fig. 1(a), that translates into the alternation between dips and peaks of the expected HOM interferogram. While the cases $\ell = 0$ and $\ell = 1$ have already been explored in the last two subsections, in Fig. 5, we present experimental data for the five cases $\ell = 0, 1, 2, 3, 4$, in which we directly show this alternation between dips and peaks, which is controlled by the projected single-photon topological charge ℓ . In Fig. 5(b) we present the measured HOM interferogram, as displayed with black circles, squares, and triangles for $\ell = 0, 2, 4$ (which lead to dips), respectively, and with red squares and triangles for $\ell = 1, 3$ (which lead to peaks), respectively. Note that while these measurements correspond to summing up all pixels on the ICCD sensor, a measurement taken on a single pixel, as displayed in Figs. 3 and 4, would exhibit a similar structure, as was also the case in the earlier figures. The black and red curves are fits to sinc-squared dip/peak profile functions, and we indicate the interference visibility attained from each of the five interferograms. In Fig. 5(a) we show, for a delay value corresponding to $\tau = -186 \text{ fs}$ ($\Delta z = -56 \mu\text{m}$), which lies outside of the dip/peak area, spatially resolved HOM interferograms for each of the cases $\ell = 0, 1, 2, 3, 4$. Note that while the case $\ell = 0$ is consistent with a

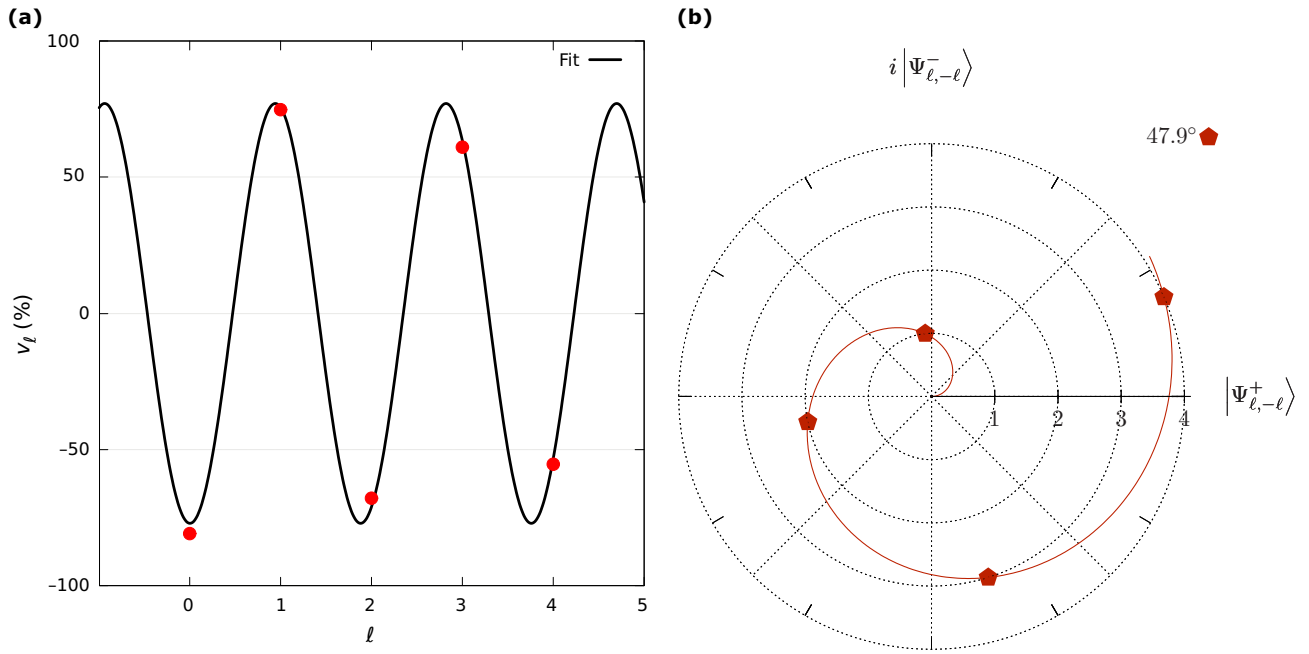


FIG. 6. (a) The red dots indicate the observed visibility for the HOM interferograms from the previous figure, while the curve indicates the best fit to the relationship in Eq. (6), yielding an interprism angle of $\phi = 47.9^\circ$. (b) Spiral polar diagram plotted for $\ell_p = 0$ and $\phi = 47.9^\circ$.

Gaussian transverse structure, the cases $\ell = 1, 2, 3, 4$ present a “doughnut” shape that is consistent with a phase singularity and the presence of OAM, as expected. Note further that the radius of the intensity distribution grows with ℓ , as is expected for an $|\ell\rangle$ mode (which corresponds to a radial superposition of Laguerre-Gaussian modes).

From an analysis of Fig. 5, it becomes evident that the visibility obtained in the experiment decreases with increasing ℓ . This is in contrast with the expectation derived from the curve marked with red pentagons in Fig. 1(a), in which the observed perfect symmetry (antisymmetry) should lead to ideal positive (negative) visibilities. It turns out that this discrepancy is due to a slight error with respect to the intended value of $\phi = 45^\circ$ in the actual value of the interprism angle ϕ . To clarify this, in Fig. 6(a), we plot the visibilities v as a function of ℓ as percentages, along with a best fit to

$$v = v_0(2 \sin^2((2\ell - \ell_p)\phi) - 1), \quad (6)$$

where $\ell_p = 0$ and v_0 represents a scaling factor. Note that while of course ℓ only takes integer values, it becomes convenient to plot this fit as a function of a real-valued ℓ . From such a fit, we obtain an estimate of the actual interprism angle ϕ in the experiment as $\phi = 47.9^\circ$, i.e., exhibiting a 2.9° experimental error. Interestingly, the fitted curve shows an excellent overlap with each of the five visibilities for $\ell = 0, 1, 2, 3, 4$. In Fig. 6(b), we present a polar spiral diagram for this adjusted ϕ value, similar to those shown in Fig. 1, further clarifying how the slight error in ϕ leads

to discrepancies with the expected perfect-state symmetry or antisymmetry.

D. Symmetry-enhanced quantum imaging

In this paper, we have demonstrated the ability to experimentally determine the HOM interferogram for each individual pixel of the ICCD sensor array, leading to the possibility of comparing its behavior to that of the global interferogram obtained by summing over all pixels. Note that in the experimental configurations presented so far, each single-pixel interferogram is essentially identical to the corresponding global interferogram; however, it becomes possible to envision a class of experiments in which the postselected state is explicitly engineered to exhibit different types of symmetry in distinct regions of the transverse plane. This would in turn translate into a single-pixel HOM interferogram that can reveal structural differences in traversing from one region to another. In this case, we would now generally expect a mismatch between the single-pixel and global interferograms.

In our experimental situation, a postselected state with differing symmetry properties across a number of regions on the transverse plane can be attained through the use of a phase mask that projects to different ℓ values depending on the transverse region. We have developed a proof-of-concept demonstration of this idea based on a bimodal phase mask defined with two regions: (i) within and (ii) outside of a chosen circumference, with an interprism angle $\phi = 45^\circ$ and a Gaussian pump mode ($\ell_p = 0$).

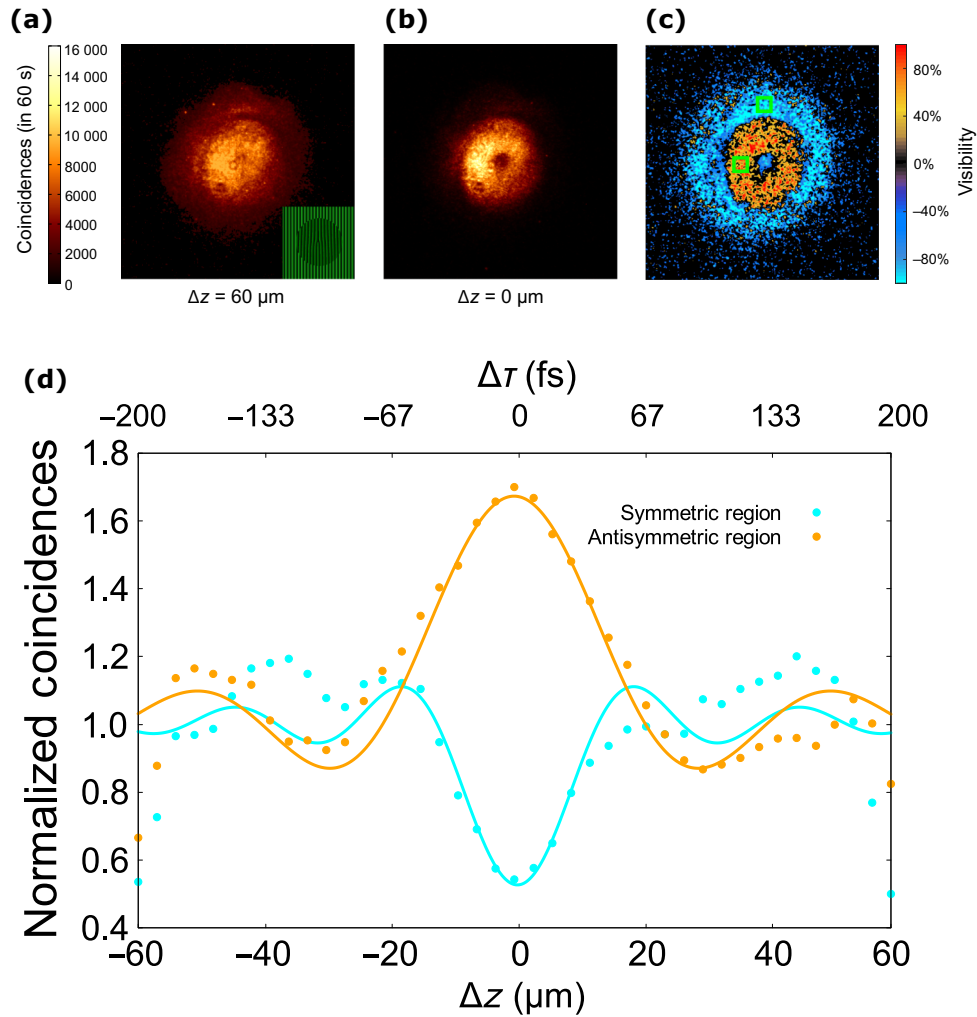


FIG. 7. HOM interference behavior for $\ell_p = 0$ and an SPDC topological charge projected in a spatially selective manner to $\ell = 1$ within a circumference on the SLM plane and to $\ell = 0$ outside of this circumference [see inset of panel (a)]. We show the spatially resolved HOM interferograms for two values of temporal delay, corresponding to (a) $\Delta z = 60 \mu\text{m}$ ($\tau = 200$ fs) and (b) $\Delta z = 0 \mu\text{m}$ ($\tau = 0$ fs). The resulting HOM visibility is shown in panel (c), with positive (negative) values in the internal (external) region. In panel (d), we show the interferograms resulting from adding up the pixels in the two regions denoted by green boxes in panel (c), showing a peak for the internal region and a dip for the external region.

In region (i), we project to $\ell = 1$, leading to an antisymmetric state; however, in region (ii), we project to $\ell = 0$, leading to a symmetric state. The actual phase mask employed in this proof-of-principle test is displayed in the inset of Fig. 7(a).

Figure 7 shows an experimental characterization of our bimodal phase mask and the resulting position-dependent symmetric or antisymmetric state. Figures 7(a) and 7(b) show the spatially resolved interferograms at two distinct temporal delay values: $\Delta z = 60 \mu\text{m}$ ($\tau = 200$ fs), i.e., outside of the interference area, and $\Delta z = 0$ ($\tau = 200$ fs) at the point of maximum interference, respectively. In going from panel (a) to panel (b), HOM interference has the effect of visibly reducing the count rate in the external region (null in coincidences, as expected for a symmetric state),

while enhancing the count rate in the internal region (peak in coincidences, as expected for an antisymmetric state). From these internal and external coincidence-count values, one may compute the position-dependent visibility according to Eq. (6), as shown in Fig. 7(c). Note that on this last plot, the two regions become easily distinguished with positive (negative) visibilities in the internal (external) regions. The fact that the dynamic range for the visibility spans -1 to 1 —as compared to the normalized count rate which spans the range 0 to 1 —leads to an enhanced contrast when comparing the two regions; this could be useful as part of a quantum imaging method. To further illustrate this photon-pair symmetry engineering protocol, we have chosen two square areas containing 3×3 pixels in the internal and external regions, as indicated by green squares

in panel Fig. 7(c). Figure 7(d) shows the HOM interferograms resulting from adding the count rate in all nine pixels within each of the two indicated squares, further clarifying that while the internal region leads to local-state antisymmetry and a peak in coincidences, the external region leads to local-state symmetry and a null in coincidences. Note that we experimentally verified that if a single pixel were to be used, the same structure is obtained for the interferograms (data not shown here), albeit naturally with more noise.

In this experimental work, we have thus demonstrated the ability to engineer the postselected two-photon state to exhibit different types of symmetry, leading to a position-dependent interference dip or peak across different transverse regions. Interestingly, while the photon-pair state remains the same across the different experimental variations reported in this paper, postselection in the form of OAM projection—and particularly position-dependent OAM projection—effectively engineers the portion of the state that participates in the measured HOM interference. Although we have employed two regions in this proof-of-principle demonstration, it is theoretically possible to scale this approach to a larger number of regions. This could play a role in quantum communication or quantum key distribution protocols, in which the position-dependent symmetry could be used as a means to encode information on the transverse plane.

IV. CONCLUSIONS

We have reported on an experiment based on photon pairs entangled in OAM, produced by the process of SPDC. The signal photon from each pair is transmitted through a sequence of two Dove prisms with a certain angle ϕ between them. This has the effect of exerting a symmetry transformation on the photon pair, for example, the conversion of a symmetric Bell state $|\Psi^+\rangle$ to an antisymmetric state $|\Psi^-\rangle$. The two photons are then allowed to interfere at a beam splitter in a HOM arrangement, with a controllable temporal delay. While the photon emanating from one of the output ports of the beam splitter is spatially resolved at an ICCD, the photon emanating from the other output port is projected to a particular topological charge ℓ through a spatial light modulator that selectively converts light traveling with topological charge ℓ to a Gaussian mode $\ell = 0$, which then couples well to a single-mode fiber.

In our experimental design, both the type of symmetry in the photon pairs and the resulting HOM interference are determined by three user-controlled parameters: the selected topological charges of the pump and SPDC photons, ℓ and ℓ_p , and the interprism angle ϕ . We have developed a polar spiral diagram, which is drawn for a given ℓ_p and elucidates the relative weights of the symmetric and antisymmetric state components, as dependent on ℓ

and ϕ (see Fig. 1). For a given experimental configuration, as determined by ℓ_p , ℓ , and ϕ , we can obtain the HOM interferogram for a single ICCD pixel or obtain the global interferogram by summing over all pixels. Note that since the HOM interference is resolved in OAM, we can freely project onto a specific ℓ in a postinterference manner.

For our measurements, we selected an interprism angle $\phi = 45^\circ$ and a Gaussian pump ($\ell_p = 0$). We first presented data showing coincident single-pixel and global HOM interferograms for $\ell = 0$ (leading to a symmetric state and an interference dip) and for $\ell = 1$ (leading to an antisymmetric postselected state and an interference peak). We also presented global HOM interferograms for all ℓ values in the range $0 \leq \ell \leq 4$, showing the alternation between dips (for $\ell = 0, 2, 4$) and peaks (for $\ell = 1, 3$). Finally, we explored a case in which we project to OAM in a spatially selective manner: to $\ell = 1$ within a certain circumference on the SLM plane, and to $\ell = 0$ outside of this circumference. We selected two 3×3 -pixel areas, one in the internal region and another in the external region, and added up all pixel readout values to obtain a separate interferogram for each of these regions, obtaining as expected a peak (indicating antisymmetry) for the internal region and a dip (indicating symmetry) for the external region. We have thus demonstrated the ability to experimentally define two transverse regions with different symmetry properties. Note that while we have defined two regions in this work, in principle, this could be scaled to a larger number of regions. We hope that the method demonstrated here for engineering the photon-pair symmetry in a spatially selective manner will be of use for future quantum technologies in the photonic domain.

ACKNOWLEDGMENTS

This work was funded by the Consejo Nacional de Ciencia y Tecnología (CF-2019-217559); PAPIIT-UNAM (IN103521) and AFOSR (FA9550-21-1-0147).

J.C.-R., P.Y.-G., and Z.I.-B. carried out the experiments. J.C.-R., R.R.-A., and Z.I.-B. carried out the data analysis. J.C.-R., P.Y.-G., R.R.-A., and Z.I.-B. developed the main conceptual ideas and physical interpretation. A.U., R.R.-A., and Z.I.-B. led the manuscript writing. A.U. and R.R.A. contributed to analysis and manuscript writing. R.R.A. directed and supported the project.

APPENDIX: VISIBILITY OF INTERFERING SYMMETRIC AND ANTISYMMETRIC OAM-ENTANGLED TWO PHOTON STATES

We are interested in obtaining an expression for the HOM interference visibility that properly takes into account the symmetric and antisymmetric state components of the SPDC photon-pair state resulting from transmission through a Dove-prism pair. Let us start this

derivation from the two-photon state prior to reaching the beam splitter, where interference occurs [18]:

$$|\Psi\rangle = \sum_{\ell} a_{\ell} \left(\cos((2\ell - \ell_p)\phi) |\Psi_{\ell, \ell_p - \ell}^+\rangle + i \sin((2\ell - \ell_p)\phi) |\Psi_{\ell, \ell_p - \ell}^-\rangle \right), \quad (\text{A1})$$

in which $\ell_p, \ell_s = \ell$, and $\ell_i = \ell_p - \ell$ are the values of the topological charge for the pump (p), signal (s), and idler (i) photons and where $|\Psi_{\ell, \ell_p - \ell}^+\rangle$ and $|\Psi_{\ell, \ell_p - \ell}^-\rangle$ are symmetric and antisymmetric Bell-state components, respectively.

HOM interference at a beam splitter (BS) acts as symmetry filter in the sense that, after the BS, the symmetric part of the SPDC state Eq. (A1) does not contribute to the coincidence rate when the photons are temporally overlapped ($\tau = 0$ fs). Specifically, the symmetric part $|\Psi_{\ell, \ell_p - \ell}^+\rangle \xrightarrow{\text{SymmetryFilter}} 0$, while the antisymmetric part remains unaltered $|\Psi_{\ell, \ell_p - \ell}^-\rangle \xrightarrow{\text{SymmetryFilter}} |\Psi_{\ell, \ell_p - \ell}^-\rangle$. Therefore, upon application of the symmetry filter, the SPDC two-photon state retains only the antisymmetric component and can be written as [25]

$$|\Psi\rangle = \sum_{\ell} a_{\ell} i \sin[(2\ell - \ell_p)\phi] |\Psi_{\ell, \ell_p - \ell}^-\rangle. \quad (\text{A2})$$

The coincidence count probability for temporally coincident photons ($\tau = 0$) can be calculated as the projection of the resulting normalized state over a given antisymmetric component. This is obtained when selecting a specific ℓ component with the SLM and is given by

$$p(\tau = 0) = \langle \Psi^- | \hat{n}(\ell) \hat{n}(\ell_p - \ell) | \Psi^- \rangle, \quad (\text{A3})$$

obtaining

$$p(0) = \sin^2[(2\ell - \ell_p)\phi]. \quad (\text{A4})$$

From the definition of the HOM visibility, we obtain

$$v = \frac{p(0) - p(\infty)}{p(\infty)}, \quad (\text{A5})$$

which, considering that $p(\tau \rightarrow \infty) = 0.5$ [26,27], is the statistical coincidence count probability for temporally distinguishable photons. This finally gives the desired result

$$v = \frac{\sin^2[(2\ell - \ell_p)\phi] - 0.5}{0.5} = 2 \sin^2[(2\ell - \ell_p)\phi] - 1. \quad (\text{A6})$$

Note that while negative values indicate a dip, positive values indicate a peak.

- [1] N. B. Simpson, K. Dholakia, L. Allen, and M. J. Padgett, Mechanical equivalence of spin and orbital angular momentum of light: An optical spanner, *Opt. Lett.* **22**, 52 (1997).
- [2] M. P. MacDonald, L. Paterson, K. Volke-Sepulveda, J. Arlt, W. Sibbett, and K. Dholakia, Creation and manipulation of three-dimensional optically trapped structures, *Science* **296**, 1101 (2002).
- [3] T. Otsu, T. Ando, Y. Takiguchi, Y. Ohtake, H. Toyoda, and H. Itoh, Direct evidence for three-dimensional off-axis trapping with single Laguerre-Gaussian beams, *Sci. Rep.* **4**, 4579 (2014).
- [4] M. J. Padgett and R. Bowman, Tweezers with a twist, *Nat. Photonics* **5**, 343 (2011).
- [5] Graham Gibson, Johannes Courtial, Miles J. Padgett, Mikhail Vasnetsov, Valeriy Pas'ko, Stephen M. Barnett, and Sonja Franke-Arnold, Free-space information transfer using light beams carrying orbital angular momentum, *Opt. Express* **12**, 5448 (2004).
- [6] M. Erhard, R. Fickler, M. Krenn, and A. Zeilinger, Twisted photons: New quantum perspectives in high dimensions, *Light Sci. Appl.* **7**, 17146 (2018).
- [7] J. Romero, D. Giovannini, S. Franke-Arnold, S. M. Barnett, and M. J. Padgett, in *Proc. SPIE 8542, Electro-Optical Remote Sensing, Photonic Technologies, and Applications VI, 85421S* (SPIE Security + Defence, Edinburgh, United Kingdom, 2012).
- [8] D. S. Ding, M. X. Dong, W. Zhang, S. Shi, Y. C. Yu, Y. H. Ye, G. C. Guo, and B. S. Shi, Broad spiral bandwidth of orbital angular momentum interface between photon and memory, *Commun. Phys.* **2**, 100 (2019).
- [9] M. Krenn, M. Malik, M. Erhard, and A. Zeilinger, Orbital angular momentum of photons and the entanglement of Laguerre-Gaussian modes, *Phil. Trans. R. Soc. A* **375**, 20150442 (2017).
- [10] M. Mirhosseini, O. S. Magaña-Loaiza, M. N. O'Sullivan, B. Rodenburg, M. Malik, M. P. J. Lavery, M. J. Padgett, D. Gauthier, and R. W. Boyd, High-dimensional quantum cryptography with twisted light, *New J. Phys.* **17**, 033033 (2015).
- [11] Y. Zhang, M. Agnew, T. Roger, F. S. Roux, T. Konrad, D. Faccio, J. Leach, and A. Forbes, Simultaneous entanglement swapping of multiple orbital angular momentum states of light, *Nat. Commun.* **8**, 632 (2017).
- [12] Z. F. Liu, C. Chen, J. M. Xu, Z. M. Cheng, Z. C. Ren, B. W. Dong, Y. C. Lou, Y. X. Yang, S. T. Xue, Z. H. Liu, W. Z. Zhu, X. L. Wang, and H. T. Wang, Hong-Ou-Mandel interference between two hyperentangled photons enables observation of symmetric and antisymmetric particle exchange phases, *Phys. Rev. Lett.* **129**, 263602 (2022).
- [13] M. Hiekkamäki and R. Fickler, High-dimensional two-photon interference effects in spatial modes, *Phys. Rev. Lett.* **126**, 123601 (2021).
- [14] H. Ling, C. Xiyue, C. Yuanyuan, and C. Lixiang, Hong-Ou-Mandel interference of spin-orbit hybrid entangled photons, *APL Photonics* **8**, 126103 (2023).
- [15] D. Cui, X. L. Wang, X. X. Yi, and L. P. Yang, Control of quantum coherence of photons exploiting quantum entanglement, *Phys. Rev. Appl.* **21**, 024019 (2024).

- [16] C. Dianzhen, Y. Xuexi, and Y. Li-Ping, Quantum imaging exploiting twisted photon pairs, *Adv. Quantum Technol.* **6**, 2300037 (2023).
- [17] Z. Ibarra-Borja, C. Sevilla-Gutiérrez, R. Ramírez-Alarcón, Q. Zhan, H. Cruz-Ramírez, and A. B. U'Ren, Direct observation of OAM correlations from spatially entangled bi-photon states, *Opt. Express* **27**, 25228 (2019).
- [18] Y. Zhang, F. S. Roux, T. Konrad, M. Agnew, J. Leach, and A. Forbes, Engineering two-photon high-dimensional states through quantum interference, *Sci. Adv.* **2**, e1501165 (2016).
- [19] A. Babazadeh, M. Erhard, F. Wang, M. Malik, R. Nouroozi, M. Krenn, and A. Zeilinger, High dimensional single photon quantum gates: Concepts and experiments, *Phys. Rev. Lett.* **119**, 180510 (2017).
- [20] X. Gao, M. Erhard, A. Zeilinger, and M. Krenn, Computer-inspired concept for high-dimensional multipartite quantum gates, *Phys. Rev. Lett.* **125**, 050501 (2020).
- [21] N. Bornman, M. Agnew, F. Zhu, A. Vallés, A. Forbes, and J. Leach, Ghost imaging using entanglement-swapped photons, *npj Quantum Inf.* **5**, 63 (2019).
- [22] N. Bornman, P. Shashi, A. Vallés, J. Leach, and A. Forbes, Ghost imaging with engineered quantum states by Hong–Ou–Mandel interference, *New J. Phys.* **21**, 073044 (2019).
- [23] Z. Y. Ou, J.-K. Rhee, and L. J. Wang, Photon bunching and multiphoton interference in parametric down-conversion, *Phys. Rev. A* **60**, 593 (1999).
- [24] Z. Ibarra-Borja, C. Sevilla-Gutiérrez, R. Ramírez-Alarcón, H. Cruz-Ramírez, and A. B. U'Ren, Experimental demonstration of full-field quantum optical coherence tomography, *Photonics Res.* **8**, 51 (2020).
- [25] Y. Zhang, F. S. Roux, T. Konrad, M. Agnew, J. Leach, and A. Forbes, Supplementary Materials for: Engineering two-photon high-dimensional states through quantum interference, *Sci. Adv.* **2**, e1501165 (2016).
- [26] A. M. Brańczyk, Hong-Ou-Mandel interference, *ArXiv*: 1711.00080.
- [27] R. Jin, Z. Zeng, C. You, and C. Yuan, Quantum interferometers: Principles and applications, *ArXiv*:2310.16378.